Reconfigurable low-emissivity optical coating using ultra-thin phase change materials

Nathan Youngblood[*,1,3], Clément Talagrand[2], Benjamin F. Porter[1], Carmelo Guido Galante[4], Steven Kneepkens[4], Graham Triggs[2], Syed Ghazi Sarwat[1], Dmitry Yarmolich[5], Ruy S. Bonilla[1], Peiman Hosseini[2], Robert A. Taylor[6], and Harish Bhaskaran*[*,1]*

[1]Department of Materials, University of Oxford, Oxford, OX1 3PH, UK
[2]Bodle Technologies Ltd., Begbroke, OX5 1PF, UK
[3]Department of Electrical and Computer Engineering, University of Pittsburgh, Pittsburgh, PA, 15261 USA
[4]Eckersley O'Callaghan Ltd, London, WC1X 8HB, UK
[5]Plasma App Ltd., Didcot, OX11 0QX, UK
[6]Department of Physics, University of Oxford, Oxford, OX1 3PJ, UK

*E-mail: *nathan.youngblood@pitt.edu* and *harish.bhaskaran@materials.ox.ac.uk*

Abstract

A method for controlling the optical properties of a solid-state film over a broad wavelength range is highly desirable and could have significant commercial impact. One such application is smart glazing technology where near-infrared solar radiation is harvested in the winter and reflected it in the summer—an impossibility for materials with fixed thermal and optical properties. Here, we experimentally demonstrate the first spectrally tunable, low-emissivity coating using a chalcogenide-based phase-change material ($Ge_{20}Te_{80}$) which can modulate the solar heat gain of a window while maintaining neutral-colouration and constant transmission of light at visible wavelengths. We additionally demonstrate the controlled transfer of absorbed near-infrared energy to far-infrared radiation which can be used to heat a building's interior and show fast, sub-millisecond switching using transparent electrical heaters integrated on glass substrates. These combined properties result in a smart window that is efficient and aesthetically pleasing—crucial for successful adoption of green technology.

Keywords: phase-change materials, energy efficiency, smart windows

Introduction

Maintaining pleasant temperatures for indoor environments consumes large amounts of energy, accounting for 20% to 40% of the national energy budgets in developed countries[1,2]. Carbon emissions associated with interior heating, cooling, and lighting are particularly high in regions of the globe that experience large swings in the environmental temperature throughout the year—comprising over 12% of total CO_2 emissions in the UK[3,4], 14% in the US[5], and as much as 30% globally[6]. Windows account for a significant fraction of the external surface area of many buildings, and therefore energy loss. During colder months, a significant amount of heat is lost through windows in the winter season—as much as 25% in the US and UK and up to 50% in northern China[7,8]. In warmer months, on the other hand, windows transmit unwanted near-infrared solar energy which heat a building's interior, causing an unnecessary load on the cooling system. Upcoming legislation, such as the EU 2021 "nearly zero-energy buildings" regulation[9], will require smart solutions to this problem that provide significant energy savings without sacrificing aesthetic appeal.

These important reasons have motivated the active research and development of dynamic glass products over the last few decades which seek to optimize energy savings, privacy, visual appeal, and comfort of a building's occupants[10,11]. Compared to static window solutions with fixed optical properties—such as low-emissivity (or "Low-E") coatings which reduce the total heat transfer through a window[12] but cannot be actively switched to make use of near-infrared solar energy in winter months—dynamic solutions are expected to reduce annual energy consumption due to heating, cooling, and lighting by as much as 8%–14% depending on the climate[13–15]. Dynamic windows generally fall into one of two categories, namely active (e.g. electrochromic, chemochromic, polarized particles, etc.) or passive (e.g. thermochromic and photochromic). While passive approaches have many practical advantages including no energy consumption during operation[16–18], lower fabrication costs,

long lifetime, and easy installation[11], the lack of direct control over the optical properties can sometimes lead to net-energy costs, rather than savings, for buildings in temperate climates[19].

Active smart glazings have the distinct advantage of direct control over the window's optical properties which can be optimized for energy efficiency or visual comfort according to both the solar and thermal conditions throughout the day. Most mature and effective amongst these active technologies are electrochromic (EC) glasses using redox reactions to reversibly control the optical transmission of the window[20]. Ion accumulation or depletion in the EC layer modulates the transmission in response to an electric field applied between two transparent conductive electrodes. Because of this, EC smart windows have response times which are limited by the motion and diffusion of ions into the active layer[21]. Additionally, EC glass usually causes attenuation over the entire solar spectrum upon switching[22,23], though recent advances in material science and nanotechnology has demonstrated spectrally selective switching in the visible and near-infrared is possible[24]. Other active designs which do not rely on the movement of ions, such as liquid crystal[25] and suspended particle devices[26–28], allow much faster switching times than EC's (a few seconds or less), but modulate the optical transmission via scattering and therefore are diffuse or tinted in the off state[26,28,29].

Here, we experimentally demonstrate an active thin-film, low-emissivity glazing that enables control over absorption of the near-infrared solar spectrum without an undesirable variation in opacity upon transition. To achieve optical modulation, we use $Ge_{20}Te_{80}$, a bi-stable, phase-change material (PCM), which has formerly been explored for use in non-volatile electronic memory[30–32], RF switches[33,34], and tunable optical devices[35–37]. Through energy transfer via optical absorption and thermal re-emission, we harvest near-infrared energy during the winter and re-emit it as far-infrared blackbody radiation. This process enables additional benefits, such as directional emission where absorbed solar energy is preferentially radiated into the building while preventing internal heat from escaping. Our

unique approach could have broad application in the design of future smart windows and energy efficient buildings[38].

Smart glazing concept and design

The concept of our smart window design is illustrated in **Fig. 1a** where a smart glazing containing ZnS:SiO_2, Ag, and 12 nm of $Ge_{20}Te_{80}$, a chalcogenide-based phase-change material (PCM), is applied to the outward-facing side of the internal window pane. We chose Ag for its properties as a high quality broadband reflector[39] and ZnS:SiO_2 for its known material advantages as an interfacial layer in phase change optical media[40]. $Ge_{20}Te_{80}$ was chosen over other common optical PCMs (such as $Ge_2Sb_2Te_5$ and AgInSbTe) because its melting temperature[41] and crystallization kinetics[42] can be significantly tuned by controlling the atomic ratio of Ge to Te. This makes reversible switching easier to achieve using electro-thermal switching approaches[43,44] as we later demonstrate. The optical stack was optimized for maximum modulation of near-infrared solar energy while maintaining a constant transmission for visible light (see Methods). The simulated optical spectrum for such a stack is shown in **Fig. 1c**. Remarkably, the active coating has a total thickness of less than 300 nm and has been optimized such that a significant fraction of the near-infrared solar energy is either reflected or absorbed depending on the state of the PCM. The external windowpane in **Fig. 1a** is composed of uncoated glass and is added to protect the smart glazing and reduce the convective heat transfer between the outside environment and internal climate of the building. While this extra pane is recommended to improve the efficiency of the overall unit (see Supplementary Note 5), it does not play a significant role in our window's optical response and we therefore limit our experimental efforts to the internal window containing the smart glazing.

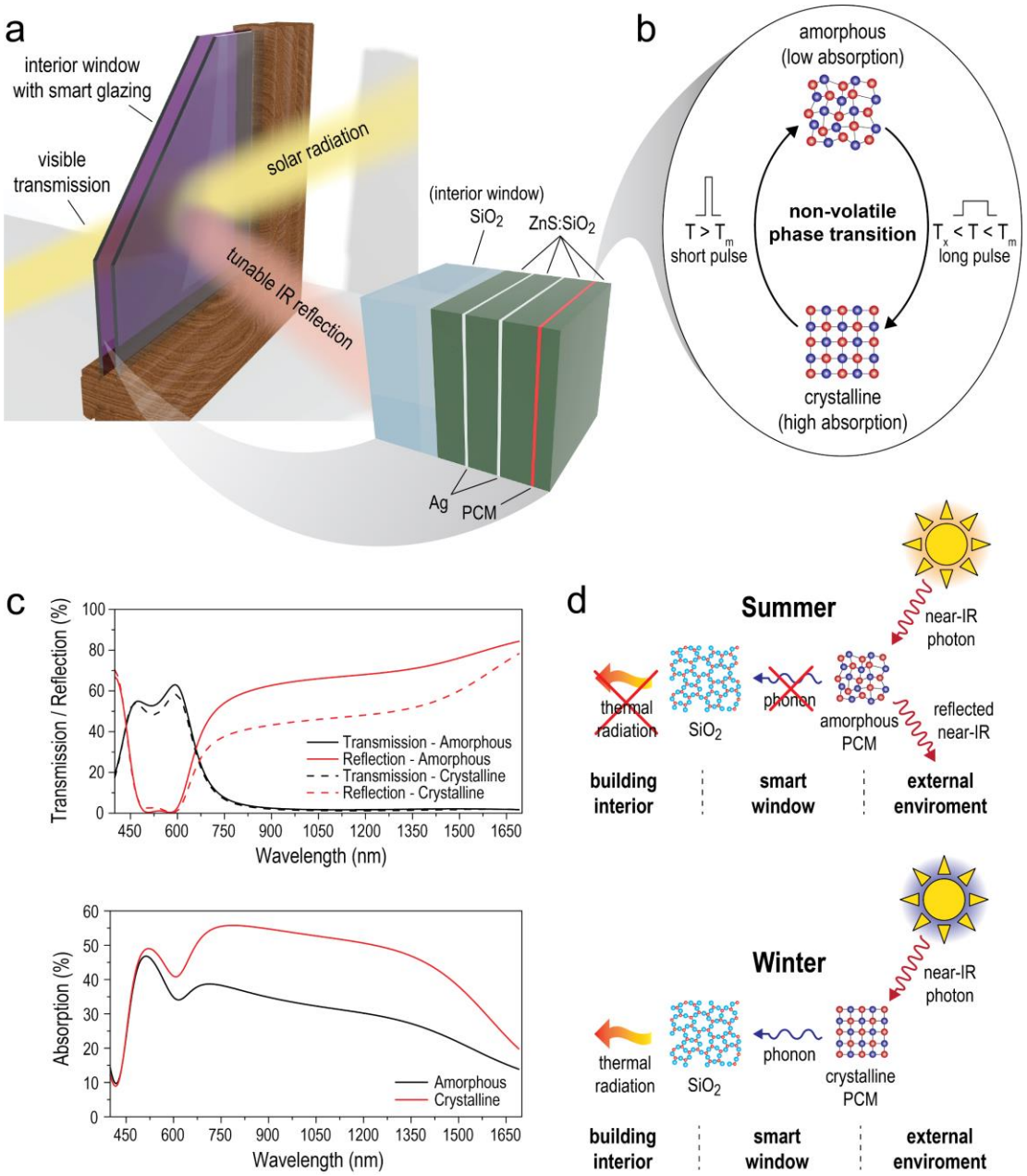

Figure 1: Phase-change smart glazing concept. a) 3D schematic of smart window design with interior windowpane containing the smart glazing layer. Solar radiation is filtered and the near-infrared is selectively reflected or absorbed. Inset: Illustration of seven-layer smart glazing optical stack containing silver, ZnS:SiO_2, and a phase-change material ($Ge_{20}Te_{80}$) layer. **b)** To initiate a phase-transition from crystalline to amorphous, a short thermal pulse greater than the melting temperature (T_m) is applied to the PCM layer via a resistive heater. A longer pulse between the crystallization (T_x) and melting temperature is used to return to the crystalline state. **c)** Simulated transmission, reflection, and absorption of smart glazing. Optical spectra were optimized for minimizing change in visible spectrum while maximizing change of absorption at near-infrared wavelengths. **d)** Concept of near-infrared absorption/thermal re-emission used in our smart window design. In winter months, near-infrared radiation from the sun is absorbed in the smart glazing layer and converted to heat. In the summer months, the PCM is switched to the amorphous phase and reflects near-infrared photons back into the external environment.

To control the transfer of near-infrared solar energy through our smart window, we make use of the significant (and non-volatile) modulation of $Ge_{20}Te_{80}$'s complex refractive

index when in the amorphous versus crystalline phase[44,45]. Here, both the real and imaginary components are modified upon crystallization resulting in increased absorption of the near-infrared spectrum. Thermally annealing the $Ge_{20}Te_{80}$ layer to a temperature above 450 °C for a short period of time before rapid quenching (less than 10 μs) randomizes the atoms in the lattice and results in an amorphous material with low near-infrared absorption (see **Fig. 1b**). Annealing for a longer time (greater than 10 μs) at a temperature of 280 °C allows $Ge_{20}Te_{80}$ to recrystallize, significantly increasing the absorption of near-infrared wavelengths. This process is non-volatile and reversible, meaning that energy is only consumed during the actual switching process and no electric field is needed to maintain either the amorphous or crystalline state[44]. Combined with the optimized Ag/ZnS:SiO_2 optical stack, energy from the near-infrared is maximally absorbed or reflected while the transmitted visible light is minimally affected (see Supplementary Note 2). In the crystalline state, the absorbed near-infrared energy is transferred to the SiO_2 glass window via phonons and re-emitted into the building through thermal radiation as illustrated in **Fig. 1d**. The high emissivity of SiO_2 and the relatively low emissivity of our optical stack (see **Fig. 3c-d**) allows for an efficient transfer of absorbed near-infrared energy to thermal radiation. Crucially, this process also allows our smart glazing to behave as a low-emissivity coating, which prevents far-infrared thermal radiation from entering or escaping the building when the PCM is in either the amorphous or crystalline state, which could potentially allow this active glazing to replace static low-e coatings while providing additional solar control (see Supplementary Note 6 for a more detailed discussion).

Spectral measurements of fabricated samples

Optical images of our fabricated smart windows are shown in both states in **Fig. 2a-c**. In **Fig. 2a**, as expected, the transmitted visible light changes very little upon phase-transition. This is a highly desirable property since significant changes in visible transmission can cause

unwanted disturbance to the building's occupants during a switching cycle[23]. Additionally, as quantified in the CIE 1931 chromaticity diagram shown in **Fig. 2d**, the colour of the transmitted light in both states remains close to the white point, which represents the visible noonday solar spectral power distribution[46]. The reflected colour shown in **Fig. 2b-c** shifts slightly toward the blue end of the colour gamut upon crystallization as wavelengths at the red end of the spectrum are more strongly absorbed.

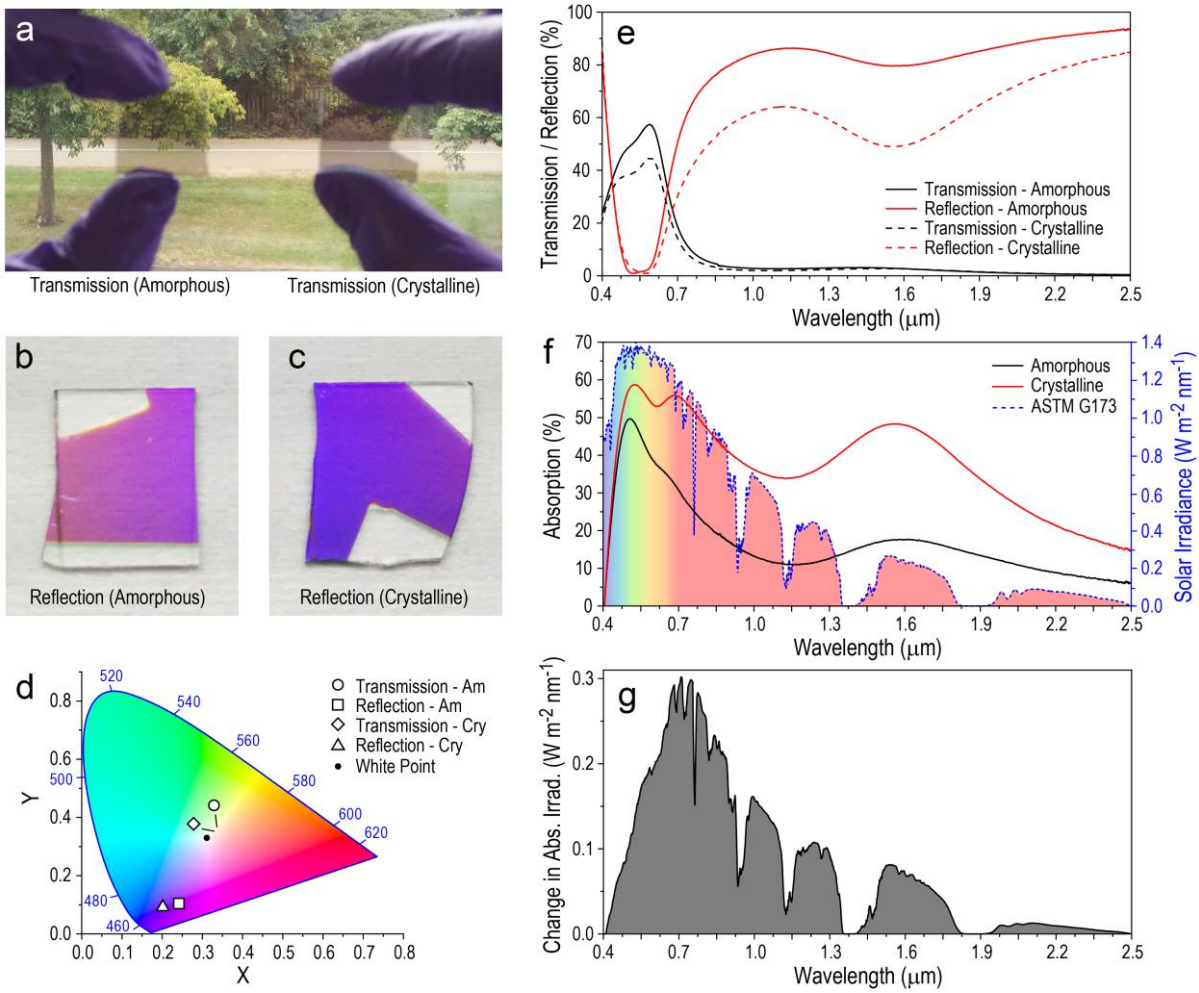

Figure 2: Experimental demonstration of phase-change smart glazing. a)-c) Optical images of transmission and reflection for fused quartz substrates with smart glazing on one side. The optical transmission is very similar regardless of the state of the PCM layer. **d)** CIE colour map of experimentally measured transmission and reflection from samples shown in **a)**. Calculated chroma for smart glazing is c* = 15.0 for amorphous transmission and c* = 8.7 for crystalline transmission relative to the white point (using the CIE Standard Illuminant D65). **e)** Measured transmission and reflection spectrum of smart glazing in both the amorphous and crystalline state. **f)** Calculated absorption spectrum from **e)** plotted with the AM1.5 solar irradiance spectrum in blue. The change in absorption is broadband and covers the entire near-infrared region. **g)** Change in absorbed solar irradiance between the amorphous and crystalline states of the smart glazing.

The optical response over the entire solar spectrum is visualized in **Fig. 2e** where we plot the transmission and reflection spectra of the smart glazing when the PCM is in both the amorphous and crystalline state. We observe relatively uniform transmission in the visible (approximately 50% transmission on average), while showing broadband modulation in the reflection of near-infrared wavelengths. Whilst the visible transmission of our smart glazing leaves room for improvement, we note that our values approach those of commercially available electrochromic smart windows in their fully transmissive state (values ranging from 60% to 80% have been reported[10,22,23]). As the transmission of the near-infrared is below 5% in both states, we attribute the observed change in reflection to increased absorption when the PCM is in the crystalline state (see Supplementary Note 1). We calculate the absorption spectra of our smart glazing in both states ($A = 1 - T - R$, where A, T, and R are the absorption, transmission, and reflection spectra respectively) and plot them against the ASTM G173 solar irradiance standard for an air mass of AM1.5g in **Fig. 2f**. Here we see that while the absorption is relatively high at visible wavelengths, the majority of absorption change occurs in the near-infrared. Crucially, the absorption in the near-infrared is low when the glazing is in the amorphous state which minimizes the amount of unwanted solar energy that is transferred to the building's interior during summer months. We plot the change in absorbed solar irradiance in **Fig. 2g** and show that the majority of the modulated energy occurs at wavelengths greater than 700 nm which have no benefit to illuminating a building's interior. Integrating the curves shown in **Fig. 2e-f** and weighting by the solar irradiance we find that 82% of unwanted near-infrared energy (780 nm to 2.5 μm) is reflected in the amorphous state while 42% is absorbed or transmitted in the crystalline state.

Energy transfer through thermal engineering

To demonstrate that the absorbed near-infrared solar energy can indeed be re-emitted as far-infrared thermal radiation, we designed an experiment to image the temperature increase of our smart window when the PCM is in the amorphous and crystalline states (see **Fig. 3a**). In this experiment, we used a FLIR® thermal camera to monitor the temperature of three samples: uncoated window (fused quartz), window with the smart glazing in the amorphous state, and window with the smart glazing in the crystalline state. The uncoated sample provided a reference thermal emission by which to calibrate the thermal camera and

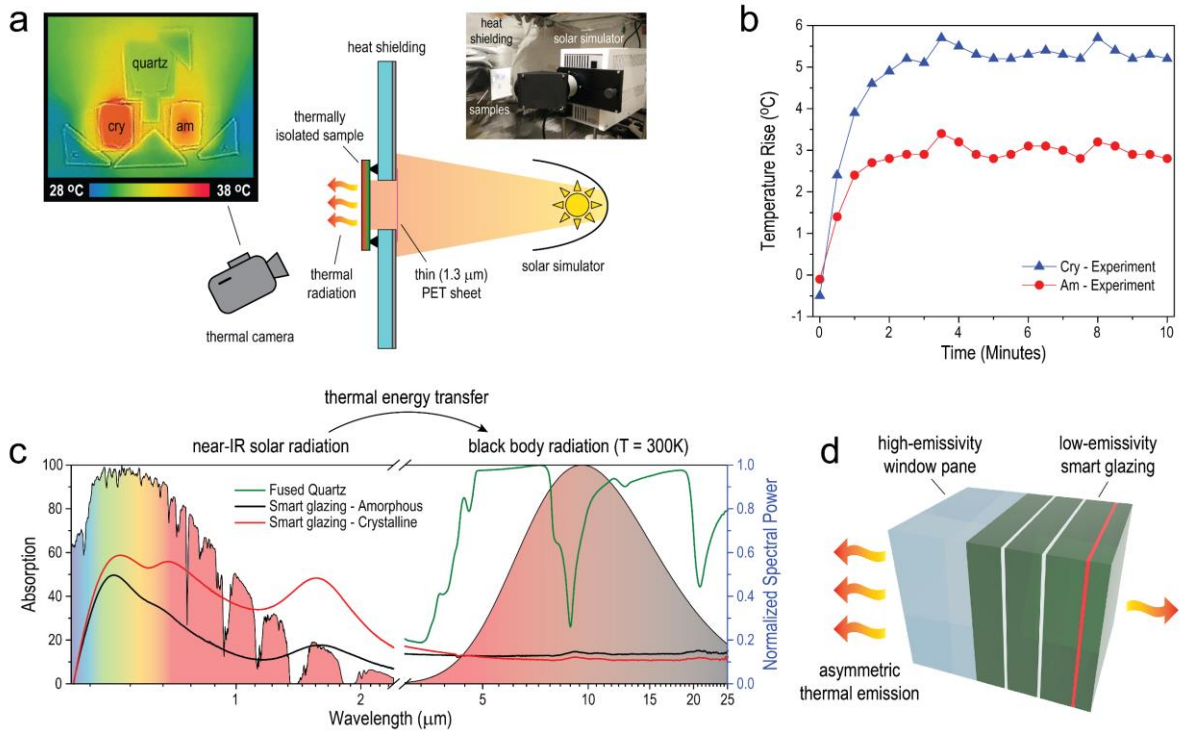

Figure 3: Demonstration of absorbed solar energy transferred to thermal radiation. a) Experimental setup used to measure temperature increase in smart glazing through near-infrared absorption. A thermal camera is used to simultaneously measure the temperature of three samples (uncoated window and windows with smart glazing in the amorphous and crystalline state) as a function of time. **b)** Measured time-dependent temperature rise in the amorphous and crystalline samples. **c)** Spectral absorption of our smart windows ranging from the visible to far-infrared as measured from the glazed and unglazed surfaces. Measurements in the range of 3 μm to 25 μm were performed using FTIR and show a significant difference in the smart glazing versus uncoated side. **d)** Illustration of asymmetric thermal emission from window with smart glazing. The low-emissivity glazing prevents harvested near-infrared energy from re-emitting back into the external environment while reducing unwanted heat transfer through the windows regardless of the PCM state.

was subtracted from the results shown in **Fig. 3b**. To illuminate the samples, we used an LOT, class ABA, solar simulator calibrated to 1 sun (1 kW/m^2) and an AM1.5g spectrum. A heat shield composed of plasterboard covered with thick aluminium foil was used to prevent unwanted thermal radiation from the simulator from saturating the thermal camera. An additional 1.3 μm thick sheet of polyethylene terephthalate (PET) was placed between the samples and the simulator which prevented additional convective heating or cooling of the samples while minimally influencing the transmitted solar spectra. **Fig. 3b** shows the temperature increase of the three samples measured every 30 seconds using the thermal camera. Both smart windows reached steady state shortly after 2 minutes of illumination with a relative 79 ± 5% increase in the temperature of the crystalline sample compared to the amorphous one. This agrees well with the percentage change (74%) in the total amount of solar energy (both visible and near-infrared) that is absorbed by the smart glazing according to the measured absorption spectra shown in **Fig. 2f**. We note that for these experiments, approximately 50% of the total sample area was obstructed from the heat shielding and sample holder. Therefore, thermal diffusion causes the temperature rise to be evenly distributed across the entire sample area, leading to an overall temperature rise of 5.3±0.1°C for the crystalline sample at steady state. This effect can be observed in Supplementary Movie 1 where the temperature rise occurs first at the sample center before diffusing to the sample edges. In samples which receive uniform solar radiation across their entire surface, we expect a factor of ~2× higher temperature than observed in **Fig. 3b**.

An additional benefit gained from re-emitting the solar spectrum as far-infrared radiation is the directional transfer of absorbed near-infrared energy through our smart window as illustrated in **Fig. 3d**. As our smart glazing is highly reflective to infrared radiation beyond 2.5 μm, we minimize the amount of harvested thermal energy which can be radiated back into the environment. On the other hand, SiO_2 performs as a highly emissive

surface at temperatures around 300 K and efficiently re-emits absorbed near-infrared radiation into the building's interior. This can be seen from the absorption spectrum in **Fig. 3c** measured on both the glass and smart glazing surfaces using Fourier-transform infrared spectroscopy (FTIR) for wavelengths between 3 µm and 25 µm. We overlay the absorption spectra with the theoretical emission spectrum of a black body at 300 K and observe significant overlap with far-infrared absorption from the glass side of the window. This overlap could be even further enhanced by adding an additional high-emissivity coating to the glass as demonstrated previously[39]. The absorption from the smart glazing side, however, remains below 20% over the entire far-infrared region in both the crystalline and amorphous states, resulting in a low-emissivity coating. This is a notable difference from other absorption-based smart window technologies (e.g. thermo- and electrochromics) which require an additional physically separated low-emissivity coating to prevent absorbed solar energy from thermally radiating into the building (see discussion in Methods and Supplementary Note 6). Due to the different emissivities of our smart window's inward- and outward-facing surfaces, near-infrared solar radiation harvested via absorption will preferentially re-emit into the building when the PCM is in the crystalline state (**Fig. 3d**). To estimate the maximum heating power of our smart glazing in the winter months due to thermal re-emission, we use the following equations (see Methods section for details):

$$P_{heat} \approx P_{abs}^{cry} - P_{rad}^{ext}(T_{ext}) = \eta_{rad} \cdot P_{abs}^{cry} \tag{1}$$

$$\eta_{rad} = \frac{\int \alpha_{FIR}^{window}(\lambda) \cdot I_{BB}(T_{int}, \lambda)\, d\lambda}{\int \left(\alpha_{FIR}^{window}(\lambda) \cdot I_{BB}(T_{int}, \lambda) + \alpha_{FIR}^{cry}(\lambda) \cdot I_{BB}(T_{ext}, \lambda) \right) d\lambda} \tag{2}$$

$$P_{abs}^{cry} = A \cos(\theta_{inc}) \int \alpha_{solar}^{cry}(\lambda) \cdot I_{solar}(\lambda, \theta, \phi)\, d\lambda \tag{3}$$

where η_{rad} is the fraction of thermal energy radiated into the building, P_{abs}^{cry} is the total solar power absorbed by the smart glazing in the crystalline state, P_{rad}^{ext} is the thermal radiation emitted back toward the outside environment, T_{int} and T_{ext} are the internal and external surface temperatures of the window, A is the area of the window, and θ_{inc} is the angle of incidence between the sun and window. $I_{BB}(T, \lambda)$ is the temperature-dependent black body spectrum and $I_{solar}(\lambda, \theta, \phi)$ is the solar spectrum of the sun for a given azimuth and altitude angles which will depend on the geographic location of the building and time of day. Using the experimentally measured values shown in **Fig. 3c** for $\alpha_{solar}^{cry}(\lambda)$ (the solar absorption of the smart glazing) and $\alpha_{FIR}^{cry}(\lambda)$, and $\alpha_{FIR}^{window}(\lambda)$ (the emissivity of both the smart glazing and uncoated sides of the window, respectively), we find $\eta_{rad} = 0.88$ and $P_{abs}^{cry}/A = 437$ W/m^2. This results in a maximum total heating power of 387 W/m^2 due to thermal emission from the window if we assume the window is installed at an angle such that it is normal to solar radiation. This corresponds to approximately 39% of the total solar energy being reradiated into the room as heat. If we include an incidence angle of $\theta_{inc} = 29.3°$ (i.e., noon on January 1st for a vertically installed, south-facing window in San Francisco, CA), the total heating power reduces to 337 W/m^2. In the summer months when the glazing is in the amorphous state, non-zero absorption in the visible and near-infrared cause a heating power of 137 W/m^2 and 83 W/m^2, respectively at normal incidence. Further work is needed to reduce this unwanted absorption when the PCM is in the amorphous state. We note that in equation (*1*) we have assumed a thermally isolated window and have neglected the effects of convection and conduction which will also serve to equilibrate the temperature difference between the glazing and surrounding air. However, when using a double-glazing configuration as we illustrate in **Fig. 1a** and analyse in detail in Supplementary Notes 5 and 7, convection will be primarily limited to the interior surface of the window (and interior of the building). Additionally, the low-emissivity smart glazing reduces the external thermal radiation

escaping or entering a building regardless of the state of the PCM, providing further energy savings throughout the year. For a more accurate estimate of the energy harvesting capabilities of our smart glazing, we have performed detailed energy savings simulations which include the full heat balance equation of the window and surrounding structure (see Supplementary Note 7).

Demonstrating reversible electrical control

In a final experiment, we demonstrated electrically controlled switching of the smart glazing by depositing our thin film stack on patterned FTO/glass substrates. For these devices, Sn-doped $G_{20}Te_{80}$ was used for the PCM layer which has comparable optical properties to $Ge_{20}Te_{80}$ (see Supplementary Note 1), but with a lower amorphization temperature[43,47,48]. The reduced melting temperature of the Sn-doped PCM allowed us to reversibly cycle the smart glazing pixel up to 1000 cycles using a transparent FTO microheater. Doping concentrations in the range of 5% to 10% atomic composition of Sn were found to sufficiently reduce the melting temperature of $Ge_{20}Te_{80}$ without introducing significant optical loss in the amorphous state. **Fig. 4a** shows the experimental setup used to observe the switching behaviour of the smart glazing pixels in real time. A broadband light source (NKT WhiteLase Micro) filtered between 1.5 and 1.6 μm using dichroic and bandpass filters was used to generate optical power in the near-infrared. The near-infrared light was then coupled to an electro-optic probe station capable of sending electrical pulses while measuring the change in optical reflection. **Fig. 4b** shows optical microscope images of a typical device before and after initial electrical switching and after 100 switching cycles. Notably, the reflected visible light is consistent in colour and intensity throughout the switching events. The electrical pulse energy was measured using an in-series 25 Ω resistor and oscilloscope. The left side of **Fig. 4c** plots the extracted pulse waveforms and switching energy for the device shown in **Fig. 4b**. The right-hand plot in **Fig. 4c** shows the switching

energy as a function of device area for multiple devices and pixel sizes. We see that while a lower peak power is required for crystallization, the total energy consumption is higher for crystallization rather than amorphization due to the longer pulse duration.

We also investigated the cyclability of our smart glazing by switching between the two states while monitoring the infrared reflection. **Fig. 4d** shows a time trace for multiple switching cycles of the device from **Fig. 4b** (time trace taken starting at 500 cycles), while **Fig. 4e-f** plot the device's cyclability and contrast for 1000 continuous cycles. Notably, we see both a reduction in the amorphous state reflection and an increase in contrast between the

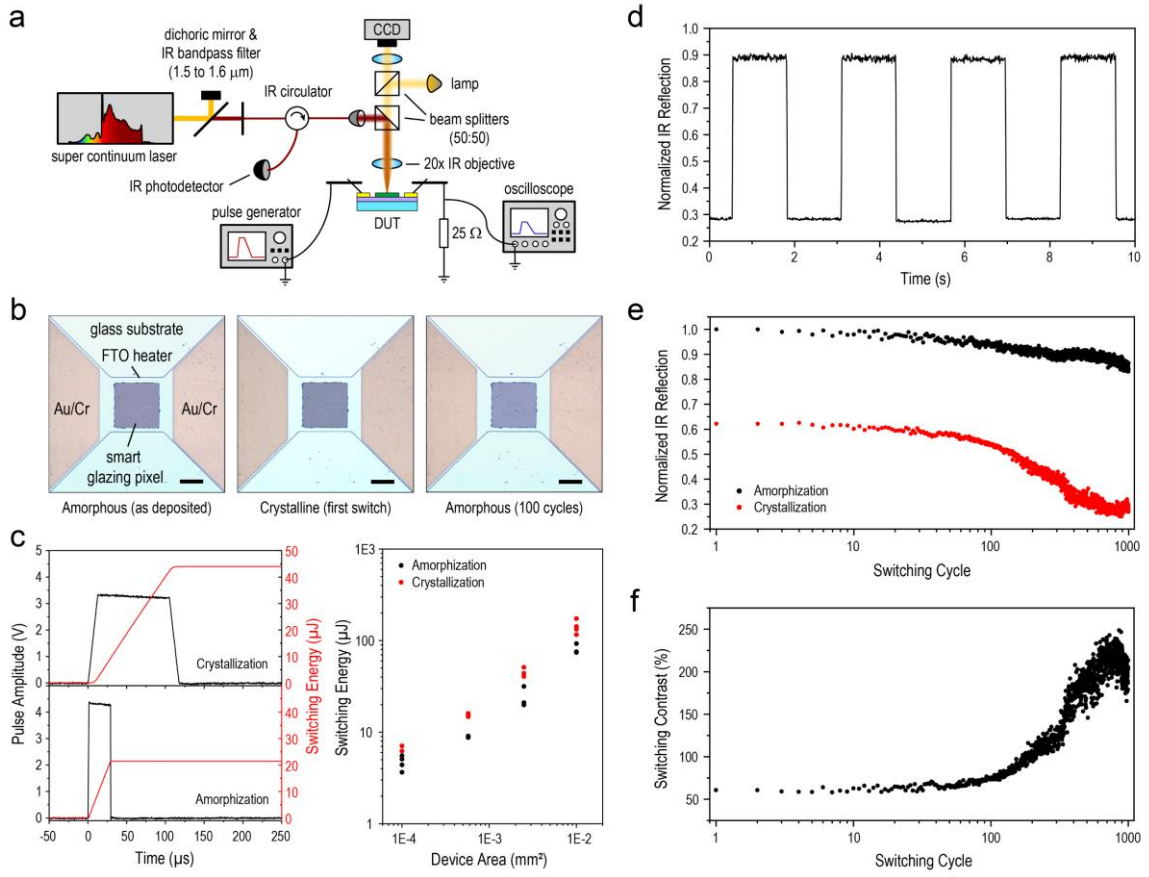

Figure 4: Electrical switching and cyclability of smart glazing pixels. a) Experimental setup used to switch the smart glazing state while measuring its reflection for wavelengths between 1.5 and 1.6 μm. **b)** Microscope images (using top and bottom illumination) of one device before switching, after first crystallization, and after 100 switching cycles (scale bar 25 μm). The visible reflection of the pixel does not vary noticeably during switching. **c)** Typical pulse shapes used to achieve crystallization and amorphization in the PCM thin film (left). Switching energy across multiple devices as a function of pixel area showing how energy scales with pixel size. **d)** Time trace of smart glazing pixel showing large near-IR contrast with fast (less than 200 μs) switching times. **e)** and **f)** Cyclability and switching contrast for device from **b)** and **c)** showing increased contrast as nucleation sites are formed.

two bi-stable states. The first is likely due to silver migration in the optical stack during thermal cycling, which results in an overall reduction of the pixel's reflectivity in both the amorphous and crystalline states[49]. The increased switching contrast, on the other hand, could be attributed to a vacancy ordering mechanism that is dependent on the annealing conditions of the PCM layer as described by Y. Zhang et al[50]. Performing a thermal annealing step before the cycling measurements could therefore improve the contrast and reliability of our devices. Indeed, for PCM memory, a "conditioning" treatment is often employed to stabilize the crystalline domain formation and improve the switching efficiency and cyclability of the memory cell[51].

Discussion

Our smart window design differs from conventional approaches, which seek to maximize the total change in solar transmission (ΔT_{solar}) inevitably leading to a significant modulation of transmission in the visible spectrum. However, by avoiding this paradigm and maximizing the total change in solar energy (including absorption and re-emission), we achieve a net annual energy savings of 17.5±5.1% across 8 different geographic locations compared to static low-e windows with similar thermal properties (see Supplementary Note 7). We note that this is achieved with a $\Delta T_{solar} = -4.4\%$, meaning in the winter months (crystalline state), the solar transmission is slightly *less* than in summer months (amorphous state). While a negative change in solar transmittance ($\Delta T_{solar} < 0$) is not ideal and leaves room for future improvement, the increase in the total solar energy absorbed and re-emitted by our crystalline PCM layer ($\Delta A_{solar} > 18\%$ see **Fig. 2f-g**) enables net energy savings in our system compared to passive low-e windows (see Methods for further discussion).

As our window primarily depends on energy harvesting from the near-infrared to heat the building's interior, the net energy savings strongly depends on the amount of sunlight

during the year (for example, see energy savings comparison between London, UK and San Francisco, CA in Supplementary Fig. S9). This limitation is ubiquitous to all active smart window approaches which maximize energy efficiency through solar modulation. Thus, it is important to consider the geographic location, window orientation, and annual weather conditions during the architectural design phase. Additionally, we note that with relatively low energy costs, the economics surrounding window supply chains is largely driven by price. Therefore, low-cost methods for patterning electrically addressable smart glazing pixels (e.g. screen printing, flexography, etc.) are needed to lower the overall cost of our approach.

In conclusion, we have demonstrated a thin-film smart glazing capable of controlling the transfer of near-infrared energy through a window using an ultra-thin phase-change active layer. This glazing provided modulation of near-infrared solar energy while maintaining a uniform transmission and colour at visible wavelengths. By absorbing near-infrared solar energy and re-emitting it as heat, we were able to demonstrate efficient harvesting of solar energy during winter months while retaining a glazing with desirable low-emissivity properties regardless of the PCM state. We then demonstrate a possible route toward integration onto glass windows using transparent electrical heaters with an initial cyclability count of 1000 cycles. Our results provide a unique and aesthetically appealing alternative to the approaches commonly used in smart window technologies and similar strategies could play an important role to reduce the carbon footprint of buildings in the future.

Methods

Solar Modulation and Design Optimization:

Using the principle of energy conservation (i.e., $T_{solar} + R_{solar} + A_{solar} = 1$), we can write the net modulation of short-wavelength solar radiation through any dynamic glazing as:

$$\Delta T_{solar} + \Delta R_{solar} + \Delta A_{solar} = 0$$

where ΔT_{solar}, ΔR_{solar}, and ΔA_{solar} are the net difference in transmission, reflection, and absorption of the solar spectrum when the window is switched between two states (e.g., amorphous and crystalline, bleached and unbleached, etc.). If the window uses only reflection or scattering to modulate solar transmission, then the change in absorption is minimal:

$$\textbf{\textit{Design \#1:}} \quad \Delta T_{solar} \approx -\Delta R_{solar} \ \text{(for } \Delta A_{solar} \ll \Delta R_{solar}\text{)}.$$

However, if a material with tunable absorption (rather than tunable reflection) is used to modulate the solar transmission, then we have:

$$\textbf{\textit{Design \#2:}} \quad \Delta T_{solar} \approx -\Delta A_{solar} \ \text{(for } \Delta R_{solar} \ll \Delta A_{solar}\text{)}.$$

In other words, a decrease in T_{solar} must accompany an equivalent increase in absorption if the reflection is held constant during modulation. This approach is commonly used by passive technologies (such as VO_2 thin films[52–54]) which require a temperature difference to initiate modulation of T_{solar} or active technologies which modulate T_{solar} via absorption (such as modulating optical extinction in plasmonic nanoparticles[55,56]). In our case, we modulate absorption and reflection to minimize the change in visible transmission through our window. Since we have designed our window to have low transmission in the near-IR and UV in both states while maintaining constant transmission in the visible, our solar modulation is ideally:

$$\textbf{\textit{Design \#3:}} \quad \Delta A_{solar} \approx -\Delta R_{solar} \ \text{(for } \Delta T_{solar} \sim 0\text{)}.$$

For all three window designs, the increased solar transmission and absorption modulates the solar heat gain coefficient (g-value) of the window glazing according to[57]:

$$\Delta g = \Delta T_{solar} + \eta_{heat}\, \Delta A_{solar}$$

where η_{heat} is the inward flowing fraction of heat that depends on the thermal properties of both the inward and outward window surfaces (thermal emissivity, convection, and conduction). Assuming a double-glazing configuration where thermal emission dominates heat transport, $\eta_{heat} \approx \eta_{rad}$ as defined in Equation (2) in the main text.

Without the addition of a low-e glazing, windows using design #2 will have a net modulation of $\Delta g = \Delta T_{solar}(1 - \eta_{heat}) \approx \Delta T_{solar}/2$ in the case of uniform thermal properties (emissivity and convection is the same on both inward and outward window surfaces). Therefore, a low-e glazing is essential for design #2 to block absorbed solar radiation from thermal re-emission into the building in summer months.

Our tunable smart glazing uses a thin PCM layer to modulate the near-infrared reflection and absorption of a low-e coating (design #3) while minimizing changes in visible transmission. From the measured spectra in **Figure 2** of the main text, we observe that when switched from amorphous to crystalline, $\Delta T_{solar} = -4.4\%$ and $\Delta A_{solar} = 18.2\%$. From the measured absorption spectra in **Figure 3c**, we estimate $\eta_{heat} \approx \eta_{rad}^{cry} = \epsilon_{glass}/(\epsilon_{glass} + \epsilon_{cry}) = 0.88$ in the crystalline state, while $\eta_{rad}^{am} = \epsilon_{glass}/(\epsilon_{glass} + \epsilon_{am}) = 0.86$ in the amorphous state. This results in a net modulation of the solar heat gain coefficient of:

$$\Delta g \approx \Delta T_{solar} + \left(\eta_{rad}^{cry} A_{solar}^{cry} - \eta_{rad}^{am} A_{solar}^{am}\right) = 12.3\%$$

To improve the performance of our design, future work is needed to optimize our glazing such that $\Delta T_{solar} \geq 0\%$ while reducing the emissivity of our window in both states such that $\eta_{rad} \approx 1$. It is also important to minimize absorption (maximize reflection) in the amorphous state in order to reduce the solar heat gain coefficient in summer months. **Table 1** outlines the key parameters needed to maximize energy savings in our approach (see Supplementary Note 7 for full energy saving simulations).

Parameter Name (All values are spectral averages at normal incidence)	**PCM Meas. (Am)**	**PCM Ideal (summer)**	**PCM Meas. (Cry)**	**PCM Ideal (winter)**
Total Solar Transmittance	21.5%	**42.1%**	17.1%	**42.1%**
Outward Solar Reflectance	52.7%	**57.9%**	38.9%	**0%**
Visible Transmittance	52.4%	**100%**	40.8%	**100%**
Outward Visible Reflectance	4.3%	**0%**	3.3%	**0%**
Inward Visible Reflectance	14.9%	**~0%**	16.5%	**~0%**
Infrared Transmittance	0%	**0%**	0%	**0%**
Outward Infrared Emissivity	0.137	**0**	0.112	**0**
Inward Infrared Emissivity	0.84	**0.84**	0.84	**0.84**

Table 1: Key parameters needed to maximize energy savings using an absorptive/reflective modulation approach.

If we assume the ideal parameters from the table above (i.e. $T_{visible} = 100\%$ and $\Delta T_{solar} = 0$), we can expect an upper bound to the modulation of Δg to be ≤ 58%. Any modulation of Δg > 58% requires modulation of both the visible and near-infrared solar spectra regardless of window design since 42% of solar radiation falls within visible wavelengths (400nm–700nm).

Optical Stack Design and Optimization:

To simulate the optical stack, we used in-house MATLAB code which simulates the optical transmission, reflection, and absorption spectra and field profile as a function of layer thickness using experimentally measured refractive indices of the thin films and the transfer matrix method approach[58]. Ag was chosen as a thin broadband reflector, while ZnS:SiO_2 was chosen due to its known material advantages as an interfacial layer in phase change optical media[40]. To make fabrication viable and minimize accumulated surface roughness, we limited our exploration to designs with 7 layers or less. We then calculated the overlap integral between the normalized ASTM-G173 solar irradiance spectrum[59] and the simulated optical spectra from the TMM approach to calculate the following figures of merit:

$$\mathrm{FOM_T} = \int_{400\ nm}^{700\ nm} T_{\mathrm{glazing\ (cry/am)}}(\lambda)\, I_{\mathrm{solar\ (norm.)}}(\lambda)\, d\lambda$$

$$\mathrm{FOM_{\Delta IR}} = \int_{750\ nm}^{2500\ nm} R_{\mathrm{glazing\ (am)}}(\lambda)\left(A_{\mathrm{glazing\ (cry)}}(\lambda) - A_{\mathrm{glazing\ (am)}}(\lambda)\right) I_{\mathrm{solar\ (norm.)}}(\lambda)\, d\lambda$$

A needle optimization technique[60] was then used to find thin film stack parameters which maximized $\mathrm{FOM_{T\ (cry)}}$, $\mathrm{FOM_{T\ (am)}}$, and $\mathrm{FOM_{\Delta IR}}$ subject to the following constraints:

- 10 nm ≤ Ag thickness ≤ 50 nm
- 7 nm ≤ GeTe thickness ≤ 50 nm
- 7 nm ≤ ZnS thickness ≤ 500 nm

The lower bound of these constraints were chosen based on the experimentally determined minimum film thicknesses that can be sputtered in our system while still preserving the optical properties of bulk films.

Estimation of Maximum Heating Power:

The heat balance equations for the external and internal surface temperatures of a window can be written[61]:

External: $P_{solar} + P_{FIR}^{ext}(T_{amb}^{ext}) - P_{rad}^{ext}(T_{ext}) + h_{ext}(T_{amb}^{ext} - T_{ext}) - k_{glass}(T_{ext} - T_{int}) = 0$

Internal: $P_{light} + P_{FIR}^{int}(T_{amb}^{int}) - P_{rad}^{int}(T_{int}) + h_{int}\left(T_{amb}^{int} - T_{int}\right) + k_{glass}(T_{ext} - T_{int}) = 0$

where these parameters can be understood as follows in **Table 2**:

Parameter	Description	Units
P_{solar}	Total solar intensity absorbed by smart glazing	[W/m^2]
P_{light}	Total optical intensity absorbed by internal window surface due to internal lighting	[W/m^2]
$P_{FIR}^{ext}(T_{amb}^{ext})$, $P_{FIR}^{int}(T_{amb}^{int})$	Thermal radiation absorbed by external and internal window surfaces	[W/m^2]
$P_{rad}^{ext}(T_{ext})$, $P_{rad}^{int}(T_{int})$	Thermal radiation emitted by external and internal window surfaces	[W/m^2]
h_{ext}, h_{int}	External and internal air film convective conductance	[W/m^2·K]
$T_{amb}^{ext}, T_{amb}^{int}$	External and internal ambient air temperatures	[K]
T_{ext}, T_{int}	External and internal surface temperatures of the window	[K]
k_{glass}	Thermal conductance of the glass	[W/m^2·K]

Table 2: List of parameters used to estimate maximum heating power.

If we add the above heat balance equations, the thermal conductance terms cancel, and we have the following equation:

$$P_{solar} + \left(P_{FIR}^{ext}(T_{amb}^{ext}) + P_{FIR}^{int}\left(T_{amb}^{int}\right)\right) - \left(P_{rad}^{ext}(T_{ext}) + P_{rad}^{int}(T_{int})\right) +$$

$$h_{ext}(T_{amb}^{ext} - T_{ext}) + h_{int}\left(T_{amb}^{int} - T_{int}\right) = 0$$

where we have assumed that for short wavelength radiation, $P_{lighting} \ll P_{solar}$ based on the relative lighting intensity and measured absorption of the internal surface of our smart

window. The total heating power of our window (P_{heat}) is the sum of both the internal radiative and convective terms:

$$P_{heat} = P_{FIR}^{int}\left(T_{amb}^{int}\right) + h_{int}\left(T_{int} - T_{amb}^{int}\right)$$

$$= P_{solar} + \left(P_{FIR}^{ext}(T_{amb}^{ext}) + P_{FIR}^{int}\left(T_{amb}^{int}\right)\right) + h_{ext}(T_{amb}^{ext} - T_{ext}) - P_{rad}^{ext}(T_{ext})$$

The radiative terms in the above equation can be found by integrating the spectral directional radiance absorbed or emitted by the window surfaces:

$$P_{solar} = \int_{\Omega} d\Omega\ \cos(\theta) \int \alpha_{solar}^{(cry/am)}(\lambda, \theta) \cdot I_{solar}(\lambda, \theta, \phi)\, d\lambda$$

$$P_{FIR}(T_{amb}) = \int_{\Omega} d\Omega\ \cos(\theta) \int \varepsilon_{atm}(\lambda, \theta) \cdot \varepsilon_{window}(\lambda, \theta) \cdot I_{BB}(\lambda, T_{amb})\, d\lambda$$

$$P_{rad}(T) = \int_{\Omega} d\Omega\ \cos(\theta) \int \varepsilon_{window}(\lambda, \theta) \cdot I_{BB}(\lambda, T)\, d\lambda$$

Here, P_{solar} is found by integrating the spectral solar irradiance absorbed by the smart glazing in either the amorphous or crystalline state. Similarly, $P_{FIR}(T_{amb})$ is the far-infrared black-body radiation emitted by the building's external or internal atmosphere and absorbed by the respective window surface. In this equation, $\varepsilon_{atm}(\lambda, \theta)$ and $\varepsilon_{window}(\lambda, \theta)$ are the spectral and directional emissivity (or absorptivity) of the air and window on either the building's exterior or interior. Finally, $P_{rad}(T)$ is the thermal radiation from the window's external or internal surface as determined by the surface emissivity and temperature. To accurately solve for P_{heat} requires full knowledge of specific building location and climate conditions and must be solved with numerical methods (see Supplementary Note 7). However, we can estimate the maximum heating power of the window due to thermal radiation by assuming the window is completely isolated from its surroundings. With this assumption, we ignore heat flow due to convection and incident thermal radiation on both window surfaces. Thus, the simplified heating power becomes:

$$P_{heat} \approx P_{rad}^{int}(T_{int}) = P_{solar} - P_{rad}^{ext}(T_{ext})$$

In equation (*1*), we have written the heating power in terms of "η_{rad}" which is the ratio of absorbed solar radiation that is emitted either toward the internal versus external environments. In the winter months, this is $P_{heat} \approx P_{rad}^{int}(T_{int}) = \eta_{rad} P_{solar}$. Thus, η_{rad} can be written as:

$$\eta_{rad} = \frac{P_{rad}^{int}(T_{int})}{P_{rad}^{int}(T_{int}) + P_{rad}^{ext}(T_{ext})}$$

which is of the same form as equation *(2)* of the main text.

Sample Fabrication:

Smart glazing films were deposited via RF/DC sputtering on double-side polished quartz wafers using a Kurt J. Lesker PVD 75 system. The base pressure was 5×10^{-7} Torr while the working pressure was 3 mTorr during deposition. RF power was 100 W and 50 W for ZnS:SiO_2 and $Ge_{20}Te_{80}$ respectively, while the DC power was 50 W for Ag. All targets were 2 inches in diameter. To ensure accurate deposition thicknesses, the film thickness was monitored in-situ using an optical monitor which was compared with a model of the optical stack, providing precise thickness control and repeatability.

To fabricate the transparent thermo-electric heaters, we purchased FTO-on-glass samples (TEC 15) from Ossila Ltd. and used photolithography and RIE etching to pattern the resistive heater shown in Fig. 4b. A 100-nm-thick electrically insulating layer of SiO_2 was then grown via PECVD to prevent electrical shorting through the PCM and Ag layers during the applied switching pulses. A second photolithography, RIE etching, and thermal evaporation process step was used to etch through the SiO_2 layer and deposit Au/Ti metal electrodes on the FTO heater. A final photolithography, sputtering, and lift-off step was used to deposit smart glazing pixels on the heaters with doped-$Ge_{20}Te_{80}$ replacing the original PCM layer.

Measurement Setup:

Transmission and reflection measurements from 400 nm to 2.5 μm were performed using a PerkinElmer Lambda 1050 UV/VIS spectrophotometer under ambient conditions. Amorphous spectra were taken of the smart glazing as deposited, while crystalline spectra were measured after a 270° C anneal on a hot plate for 15 seconds. Mid- to far-infrared absorption was measured using a Varian Excalibur FTS 3500 FTIR spectrometer operating from 3 to 25 μm. For thermal characterization, a FLIR© ONE Pro camera was used to measure the temperature rise in the uncoated quartz versus the quartz with smart glazing in the amorphous and crystalline states. The samples were illuminated with an LOT, class ABA, solar simulator calibrated to 1 sun (1 kW/m^2) and an AM1.5g spectrum. A heat shield composed of plasterboard covered with thick aluminum foil was used to prevent unwanted thermal radiation from the simulator from saturating the FLIR© thermal camera. The transmission of the 1.3 μm thick sheet of PET was also calibrated using the PerkinElmer Lambda spectrometer and factored into the calculated total solar absorption.

For reversible switching measurements, near-IR light (λ = 1.5–1.6μm) from a super-luminescent source (NKT WhiteLase Micro) was filtered using dichroic and bandpass filters and coupled to a custom built electro-optic probe station through a fiber circulator and fiber-to-free space collimator (Thorlabs 6015-3-APC and TC06APC-1550). Near-IR light was focused on the samples using a NIR objective (Mitutoyo M Plan Apo NIR 20x, 0.42 NA) and reflected light from the sample was coupled to a Newport 2011-FC photodetector through the output port of the circulator. A Tektronix AFG3102 function generator was used to send electrical pulses to the FTO devices with customizable shapes. The reflected near-IR optical signal and electrical current through the device was monitored with an oscilloscope (Lecroy 1GHz Wavesurfer) and recorded via a PC during the cyclability studies in Fig. 4d-f.

Supporting Information

This material is available free of charge via the internet at https://pubs.acs.org/.

- Details on phase-change thermal and optical properties; manufacturability and angular dependence; comparison with alternative smart window technologies; energy savings simulations; electro-thermal cycling and scalability considerations.

Correspondence and requests

Correspondence and requests for materials can be directed to NY (nathan.youngblood@pitt.edu) and HB (harish.bhaskaran@materials.ox.ac.uk).

Funding Sources

This research was supported by EPSRC via grants EP/M015173/1 (WAFT Consortium), EP/J018694/1, EP/M015130/1, and EP/M022196/1 in the UK and the National Science Foundation (NSF) via grants DMR-2003325 and ECCS-2028624 in the US.

Contributions

All authors contributed to this work. NY, PH, and HB conceptualized and developed the concept and wrote the manuscript. GSS and GT carried out some of the dynamic experiments in the work. CGG and SK carried out the modeling work on energy savings. BFP and DY aided fabrication of transparent heaters. CT and PH deposited the films on the dynamic heaters. RSB and RT helped NY with spectroscopic measurements on the films.

Conflicts of Interest

HB, PH and CT hold shares in and HB and PH serve on the Board of Directors at Bodle Technologies Limited. NY, HB, PH, CT and GSS have pending patent applications related to this technology. HB is employed at the University of Oxford which is incentivized to have papers published in top journals.

Data Availability

All data needed to evaluate the conclusions in the paper are present in the paper and/or the Supporting Information. Additional data related to this paper may be requested from the authors or Oxford Research Archive for Data (https://ora.ox.ac.uk).

References

1. Pérez-Lombard, L., Ortiz, J. & Pout, C. A review on buildings energy consumption information. *Energy Build.* **40**, 394–398 (2008).
2. Kamalisarvestani, M., Saidur, R., Mekhilef, S. & Javadi, F. S. Performance, materials and coating technologies of thermochromic thin films on smart windows. *Renew. Sustain. Energy Rev.* **26**, 353–364 (2013).
3. Brown, P. & MacCarthy, J. Sector, Gas, and Uncertainty Summary Factsheets - Greenhouse Gas Emissions. https://naei.beis.gov.uk/resources/Sector_Summary_Factsheet_2020-v2.html (accessed 2021-07-26).
4. Delay, T., Farmer, S. & Jennings, T. Building the future today. *Carbon Trust* https://www.carbontrust.com/resources/building-the-future-today (accessed 2021-7-26).
5. Kwok, A. G. & Rajkovich, N. B. Addressing climate change in comfort standards. *Build. Environ.* **45**, 18–22 (2010).
6. Energy Technology Perspectives 2015. *IEA* https://www.iea.org/reports/energy-technology-perspectives-2015 (accessed 2021-07-26).
7. Building fabric guide. *Carbon Trust* https://www.carbontrust.com/resources/building-fabric-guide (accessed 2021-07-26).
8. Rezaei, S. D., Shannigrahi, S. & Ramakrishna, S. A review of conventional, advanced, and smart glazing technologies and materials for improving indoor environment. *Sol. Energy Mater. Sol. Cells* **159**, 26–51 (2017).
9. Directive 2010/31/EU of the European Parliament and of the council on the energy performance of buildings. *Official Journal of the European Union* http://data.europa.eu/eli/dir/2010/31/oj (accessed 2021-07-26).

10. Casini, M. Active dynamic windows for buildings: A review. *Renew. Energy* **119**, 923–934 (2018).

11. Wang, Y., Runnerstom, E. L. & Milliron, D. J. Switchable Materials for Smart Windows. *Annu. Rev. Chem. Biomol. Eng.* **7**, annurev-chembioeng-080615-034647 (2016).

12. Hammarberg, E. & Roos, A. Antireflection treatment of low-emitting glazings for energy efficient windows with high visible transmittance. *Thin Solid Films* **442**, 222–226 (2003).

13. Dussault, J.-M., Gosselin, L. & Galstian, T. Integration of smart windows into building design for reduction of yearly overall energy consumption and peak loads. *Sol. Energy* **86**, 3405–3416 (2012).

14. Tavares, P., Bernardo, H., Gaspar, A. & Martins, A. Control criteria of electrochromic glasses for energy savings in mediterranean buildings refurbishment. *Sol. Energy* **134**, 236–250 (2016).

15. Aste, N., Compostella, J. & Mazzon, M. Comparative energy and economic performance analysis of an electrochromic window and automated external venetian blind. *Energy Procedia* **30**, 404–413 (2012).

16. Gao, Y. *et al.* Nanoceramic VO2 thermochromic smart glass: A review on progress in solution processing. *Nano Energy* **1**, 221–246 (2012).

17. Zhou, J. *et al.* VO2 thermochromic smart window for energy savings and generation. *Sci. Rep.* **3**, 3029 (2013).

18. Cui, Y. *et al.* Thermochromic VO2 for Energy-Efficient Smart Windows. *Joule* **2**, 1707–1746 (2018).

19. Ye, H., Meng, X. & Xu, B. Theoretical discussions of perfect window, ideal near infrared solar spectrum regulating window and current thermochromic window.

Energy Build. **49**, 164–172 (2012).

20. Cai, G., Eh, A. L.-S., Ji, L. & Lee, P. S. Recent Advances in Electrochromic Smart Fenestration. *Adv. Sustain. Syst.* **1**, 1700074 (2017).
21. Granqvist, C. G. Electrochromics for smart windows: Oxide-based thin films and devices. *Thin Solid Films* **564**, 1–38 (2014).
22. Lee, E. Application issues for large-area electrochromic windows in commercial buildings. *Sol. Energy Mater. Sol. Cells* **71**, 465–491 (2002).
23. Zinzi, M. Office worker preferences of electrochromic windows: a pilot study. *Build. Environ.* **41**, 1262–1273 (2006).
24. Llordés, A., Garcia, G., Gazquez, J. & Milliron, D. J. Tunable near-infrared and visible-light transmittance in nanocrystal-in-glass composites. *Nature* **500**, 323–326 (2013).
25. Debije, M. G. Solar Energy Collectors with Tunable Transmission. *Adv. Funct. Mater.* **20**, 1498–1502 (2010).
26. Ghosh, A., Norton, B. & Duffy, A. Measured overall heat transfer coefficient of a suspended particle device switchable glazing. *Appl. Energy* **159**, 362–369 (2015).
27. Vergaz, R., Sánchez-Pena, J.-M., Barrios, D., Vázquez, C. & Contreras-Lallana, P. Modelling and electro-optical testing of suspended particle devices. *Sol. Energy Mater. Sol. Cells* **92**, 1483–1487 (2008).
28. Barrios, D., Vergaz, R., Sanchez-Pena, J. M., Granqvist, C. G. & Niklasson, G. A. Toward a quantitative model for suspended particle devices: Optical scattering and absorption coefficients. *Sol. Energy Mater. Sol. Cells* **111**, 115–122 (2013).
29. Kim, G. W. *et al.* Next generation smart window display using transparent organic display and light blocking screen. *Opt. Express* **26**, 8493 (2018).
30. Perniola, L. *et al.* Electrical Behavior of Phase-Change Memory Cells Based on GeTe.

IEEE Electron Device Lett. **31**, 488–490 (2010).

31. Bruns, G. *et al.* Nanosecond switching in GeTe phase change memory cells. *Appl. Phys. Lett.* **95**, 043108 (2009).

32. Burr, G. W. *et al.* Phase change memory technology. *J. Vac. Sci. Technol. B, Nanotechnol. Microelectron. Mater. Process. Meas. Phenom.* **28**, 223–262 (2010).

33. Singh, T. & Mansour, R. R. Characterization, Optimization, and Fabrication of Phase Change Material Germanium Telluride Based Miniaturized DC–67 GHz RF Switches. *IEEE Trans. Microw. Theory Tech.* **67**, 3237–3250 (2019).

34. King, M. R. *et al.* Morphological analysis of GeTe in inline phase change switches. *J. Appl. Phys.* **118**, 094501 (2015).

35. Jafari, M., Guo, L. J. & Rais-Zadeh, M. Waveguide Grating Color Reflector Using Germanium Telluride. in *2019 20th International Conference on Solid-State Sensors, Actuators and Microsystems & Eurosensors XXXIII (TRANSDUCERS & EUROSENSORS XXXIII)* 478–481 (IEEE, 2019). doi:10.1109/TRANSDUCERS.2019.8808283.

36. Jafari, M., Guo, L. J. & Rais-Zadeh, M. A Reconfigurable Color Reflector by Selective Phase Change of GeTe in a Multilayer Structure. *Adv. Opt. Mater.* **7**, 1801214 (2019).

37. Polking, M. J. *et al.* Controlling Localized Surface Plasmon Resonances in GeTe Nanoparticles Using an Amorphous-to-Crystalline Phase Transition. *Phys. Rev. Lett.* **111**, 037401 (2013).

38. Ke, Y. *et al.* Smart Windows: Electro-, Thermo-, Mechano-, Photochromics, and Beyond. *Adv. Energy Mater.* **9**, 1902066 (2019).

39. Raman, A. P., Anoma, M. A., Zhu, L., Rephaeli, E. & Fan, S. Passive radiative cooling below ambient air temperature under direct sunlight. *Nature* **515**, 540–544 (2014).

40. Kim, E.-K., Kwun, S.-I., Lee, S.-M., Seo, H. & Yoon, J.-G. Thermal boundary

resistance at Ge2Sb2Te5/ZnS:SiO2 interface. *Appl. Phys. Lett.* **76**, 3864–3866 (2000).

41. Chen, M., Rubin, K. A. & Barton, R. W. Compound materials for reversible, phase-change optical data storage. *Appl. Phys. Lett.* **49**, 502–504 (1986).

42. Raoux, S., Cheng, H.-Y., Caldwell, M. A. & Wong, H.-S. P. Crystallization times of Ge–Te phase change materials as a function of composition. *Appl. Phys. Lett.* **95**, 071910 (2009).

43. Castillo, S. G. *et al.* 57-4: Solid State Reflective Display (SRD ®) with LTPS Diode Backplane. *SID Symp. Dig. Tech. Pap.* **50**, 807–810 (2019).

44. Broughton, B. *et al.* 38-4: Solid-State Reflective Displays (SRD ®) Utilizing Ultrathin Phase-Change Materials. *SID Symp. Dig. Tech. Pap.* **48**, 546–549 (2017).

45. Yamada, N., Ohno, E., Nishiuchi, K., Akahira, N. & Takao, M. Rapid-phase transitions of GeTe-Sb2Te3 pseudobinary amorphous thin films for an optical disk memory. *J. Appl. Phys.* **69**, 2849–2856 (1991).

46. Schanda, J. CIE Colorimetry. in *Colorimetry* 25–78 (John Wiley & Sons, Inc., 2007). doi:10.1002/9780470175637.ch3.

47. Lee, M. L. *et al.* Crystallization and thermal stability of Sn-doped Ge 2 Sb 2 Te 5 phase change material. *J. Phys. D. Appl. Phys.* **41**, 215402 (2008).

48. Song, W. D., Shi, L. P., Miao, X. S. & Chong, T. C. Phase change behaviors of Sn-doped Ge–Sb–Te material. *Appl. Phys. Lett.* **90**, 091904 (2007).

49. Leftheriotis, G., Yianoulis, P. & Patrikios, D. Deposition and optical properties of optimised ZnS/Ag/ZnS thin films for energy saving applications. *Thin Solid Films* **306**, 92–99 (1997).

50. Zhang, Y. *et al.* Myths and truths about optical phase change materials: A perspective. *Appl. Phys. Lett.* **118**, 210501 (2021).

51. Loke, D. K. *et al.* Ultrafast Nanoscale Phase-Change Memory Enabled By Single-

Pulse Conditioning. *ACS Appl. Mater. Interfaces* **10**, 41855–41860 (2018).

52. Zhang, Z. *et al.* Solution-based fabrication of vanadium dioxide on F:SnO2 substrates with largely enhanced thermochromism and low-emissivity for energy-saving applications. *Energy Environ. Sci.* **4**, 4290 (2011).

53. Chen, Z. *et al.* Fine crystalline VO2 nanoparticles: synthesis, abnormal phase transition temperatures and excellent optical properties of a derived VO2 nanocomposite foil. *J. Mater. Chem. A* **2**, 2718 (2014).

54. Ke, Y. *et al.* Controllable Fabrication of Two-Dimensional Patterned VO 2 Nanoparticle, Nanodome, and Nanonet Arrays with Tunable Temperature-Dependent Localized Surface Plasmon Resonance. *ACS Nano* **11**, 7542–7551 (2017).

55. Garcia, G. *et al.* Near-Infrared Spectrally Selective Plasmonic Electrochromic Thin Films. *Adv. Opt. Mater.* **1**, 215–220 (2013).

56. Barile, C. J. *et al.* Dynamic Windows with Neutral Color, High Contrast, and Excellent Durability Using Reversible Metal Electrodeposition. *Joule* **1**, 133–145 (2017).

57. Klems, J. H. A New Method for Predicting the Solar Heat Gain of Complex Fenestration Systems I. Overview and Derivation of the Matrix Layer Calculation. *ASHRAE Trans.* **100**, LBL-34715 (1994).

58. Pettersson, L. A. A., Roman, L. S. & Inganäs, O. Modeling photocurrent action spectra of photovoltaic devices based on organic thin films. *J. Appl. Phys.* **86**, 487–496 (1999).

59. NREL. Reference Solar Spectral Irradiance: Air Mass 1.5. *American Society for Testing and Materials (ASTM) Terrestrial Reference Spectra for Photovoltaic Performance Evaluation* http://rredc.nrel.gov/solar/spectra/am1.5/ (accessed 2021-07-26).

60. Tikhonravov, A. V., Trubetskov, M. K. & DeBell, G. W. Application of the needle optimization technique to the design of optical coatings. *Appl. Opt.* (1996)

doi:10.1364/ao.35.005493.

61. EnergyPlus™ Version 9.4.0 Documentation: Engineering Reference. *U.S. Department of Energy* 362–367 https://energyplus.net/documentation (accessed 2021-07-26).